Coupled electromagnetic and thermal optimisation strategies for direct-drive linear permanent magnet synchronous motors

Soroosh Haji Hosseinnejad[1], *Student Member, IEEE*, Thor F. Besier[2],
Andrew J. Taberner[2], *Senior Member, IEEE*, and Bryan P. Ruddy[2*], *Member, IEEE*

***Abstract*—We present the design and fabrication of an actively cooled direct-drive linear permanent magnet synchronous motor for a wearable assistive device. We derive a detailed thermal model of the actuator for designing an air-cooling system. We combine this thermal model with a semi-analytical electromagnetic model of the motor to optimise the efficiency of the motor. Our fabricated motor has a nominal mass of 624 g, and consumes 80 W under a 100 N load. The motor's static force production and its thermal performance were experimentally tested, suggesting that the motor can safely achieve ∼132 N/kg continuous force production at its nominal load.**

***Index Terms*—direct-drive linear permanent magnet synchronous motors, optimisation strategies, electromechanical systems.**

I. Introduction

Current robot-assisted approaches for upper limb rehabilitation appear to offer insignificant improvement over manual physiotherapy [1]. One major contributor to their ineffectiveness is that the majority of assistive robots uses heavy actuators, which are designed for industrial applications, not for interacting with humans [2]. Rotary electric motors have low torque/weight ratios and require transmission systems to increase their torque, leading to backlash, stiffness and control problems [3]. Furthermore, rotary actuated robots require complex mechanisms and control to be aligned with the variable instantaneous axes of rotation of the joint to mimic the exact kinematics of the limb [4].

Direct-drive linear electric motors, such as linear permanent magnet synchronous motors (LPMSMs) [5] or voice coils [3], are easy to control and highly backdriveable, compared to other linear technologies such as hydraulic and pneumatic actuators. However, conventional direct-drive linear motors have low thrust per unit volume [6]. Design optimisation of permanent magnet motors has been explored to increase the force density of these motors [5], [7] and [8]. However, since thermal limitations dominate the thrust capability of an electrical motor [9], the design of a cooling system for the machine becomes more and more critical [10]. There have been some reports on designing cooling systems for direct drive motors, such as an active water cooling system [11], a hydraulic pump [10] and an array of fins with a natural convection strategy [12]. However, a combined design strategy for optimising the force production and thermal performance of a direct-drive linear motor based on an analytical model has not been investigated.

We have previously reported a conceptual analysis of a pelvis-to-humerus assistive device powered by a direct-drive linear motor [13] using the demonstrated performance [11] of linear synchronous motors. In this paper, we present the design and performance of a prototype high-force direct-drive LPMSM for a shoulder assistive robot. We present the mechanical and electromagnetic design for the device (Fig. 1), followed by the design of the thermal management system required to support the required power. Finally, we experimentally evaluate the static thrust and thermal performance of the motor.

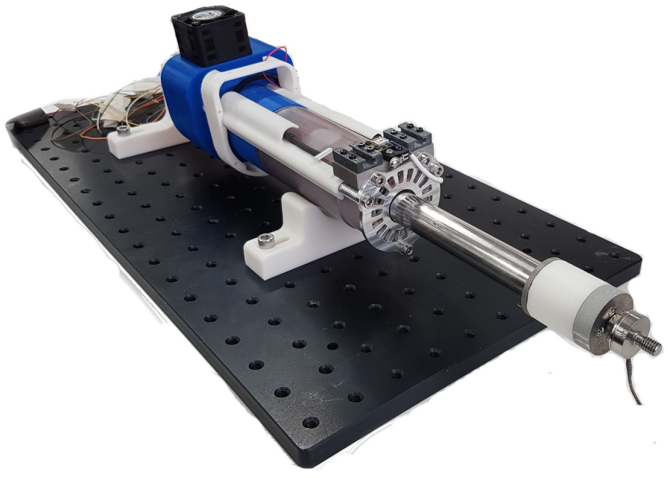

Fig. 1. Overview of the prototyped direct-drive linear motor, attached to an optical table. A load cell is attached to the motor shaft for force measurement.

This work was supported by the Medical Technologies Centre of Research Excellence, funded by the Tertiary Education Commission of New Zealand.

[1]S. Haji Hosseinnejad is with the Auckland Bioengineering Institute, University of Auckland, Auckland 1142, New Zealand (e-mail: shos997@aucklanduni.ac.nz, ldo004@aucklanduni.ac.nz).

[2]B. P. Ruddy, T. F. Besier, and A. J. Taberner are with the Auckland Bioengineering Institute and the Department of Engineering Science, University of Auckland, Auckland 1142, New Zealand (phone: +64 9 923 2424; fax: +64 9 367 7157; e-mail: t.besier@auckland.ac.nz, a.taberner@auckland.ac.nz, b.ruddy@auckland.ac.nz).

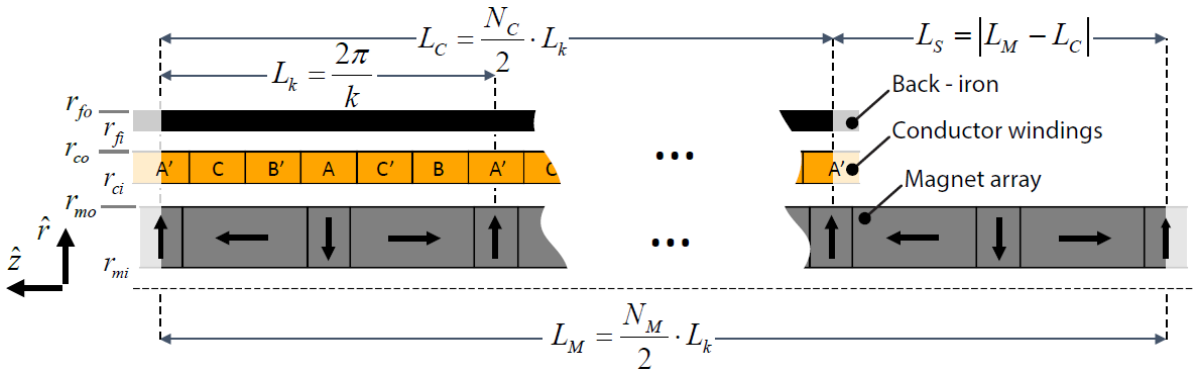

Fig. 2. Schematic of the tubular linear synchronous motor design employed here, showing the quasi-Halbach magnet array, three-phase coil structure, and exterior back-iron. (Figure adapted from [8].)

II. DESIGN OPTIMIZATION

Planar motors within a symmetric Halbach array, where magnets are arranged with a periodic, rotating direction of magnetisation along the array, offer the best magnetic field [5]. However, tubular motors are more convenient for compact packages and allow for the more efficient use of copper [11].

Therefore, a tubular quasi-Halbach motor design was selected (Fig. 2). The motor has a periodic structure of repeat length L_k, and a coil composed of fewer repeat segments than the magnet (underhung configuration) as this design approach has been previously shown to offer higher efficiency than overhung motors [14]. For ease of construction and lightweight design, the back-iron is approximately the same length as the coil and travels with it. However, as the back-iron moves with respect to the magnets, it generates cogging force.

The actuator can be designed by an electromagnetic model, outlined in [5], which essentially solves Poisson's equation in cylindrical coordinates using an analytical Fourier solution. Compared to finite element analysis (FEA) [15] and standard integral methods [16], this formulation is computationally cost efficient, and avoids the numerical instability problems common to explicit analytical solutions [17].

The motor force F can be found by determining a dimensionless force constant $\hat{F}$ [5]. This parameter was computed by employing a Fourier solution to Maxwell's equations which essentially integrates the Lorentz force over radial and axial magnetic field which crosses the motor coil. Therefore, the force generated by the motor can be described as [5]

$$F = \frac{2\pi B_{rem} J_1 N_M}{k^3} \hat{F} \tag{1}$$

where J_1 is the magnitude of the first harmonic of current density, B_{rem} is the remanent magnetization of the permanent magnet, $k = 2\pi/L_k$ and N_M is the number of magnet poles.

The model used in [5] is for a motor with a back-iron with the same size as the magnets. Therefore, the dimensionless mass parameter of the motor $\hat{M}$ in [5] is defined as follows to describe the motor as a back-iron with the same length as the coil.

$$\begin{aligned}\hat{M} = \pi \left[f + (1-f)\frac{\rho_{ins}}{\rho_c} \right] \left[(kr_{co})^2 - (kr_{ci})^2 \right] \left(\frac{N_C}{N_M} \right) \\ + \pi \left(\frac{\rho_m}{\rho_c} \right) \left[(kr_{mo})^2 - (kr_{mi})^2 \right] \\ + \pi \left(\frac{\rho_f}{\rho_c} \right) \left[(kr_{fo})^2 - (kr_{fi})^2 \right] \left(\frac{N_C}{N_M} \right)\end{aligned} \tag{2}$$

where f is the copper fill factor, ρ_{ins} and ρ_c are the winding and insulator conductor densities, respectively, ρ_m is the permanent magnet density, ρ_f is the iron density, and r_{ci} and r_{co} are the inner and outer radii of the coil, respectively. r_{mi} and r_{mo} are the inner and outer radius of the magnets respectively, and r_{fi} and r_{fo} are the inner and outer radius of the iron core, respectively. N_C is the number of coil poles [8].

With σ_c as the conductivity of the copper, the mass of the motor (M) including the magnets, coils and back-iron shell is

$$M = \frac{2\pi N_M \sigma_c}{k^3} \hat{M} \tag{3}$$

A. Thermal Model

The thermal resistance of the cylindrical coil with heat generation can be found by solving the heat diffusion equation. Assuming steady-state conduction, negligible radiation heat loss, and uniform heat generation in the coil, the thermal resistance of the coil ($R_{th,c}$) with the length of L_c and thermal conductivity of k_c, is given [11] as

$$R_{th,c} = \frac{1}{2\pi L_c \kappa_c} \left(\frac{1}{2} - \frac{\ln \frac{r_{co}}{r_{ci}}}{\left(\frac{r_{co}}{r_{ci}} \right)^2 - 1} \right) \tag{4}$$

The thermal resistance of the motor, $R_{th,tot}$, from the inner surface of the coil to the ambient via the outside of the back-iron in a cylindrical coordinate system can be written as

$$R_{th,tot} = R_{th,c} + \frac{1}{2\pi L_c} \left[\frac{\ln \frac{r_{fi}}{r_{co}}}{\kappa_{gap}} + \frac{\ln \frac{r_{fo}}{r_{fi}}}{\kappa_{iron}} + \frac{1}{r_{fo}\bar{h}} \right] \tag{5}$$

where k_{gap} is the thermal conductivity of the space between the coil and the back-iron (assumed to be filled with a thermal compound of conductivity 1 W/m·K), k_{iron} is the iron thermal conductivity (80 W/m·K) and $\bar{h}$ is the heat transfer coefficient on the outside of the back-iron.

This expression for thermal resistance reveals that a typical natural convection heat transfer coefficient of $10\,\mathrm{W/m^2K}$ results in a thermal resistance ~ 100 times higher than which is required to keep the motor at a safe operating temperature. Therefore, an array of copper fins with thickness t of 0.2 mm and a high-static-pressure DC fan were used to enhance the heat transfer (Figure 6). The number (n) and the length of the fins (L_{fin}) are calculated based on the pressure drop (ΔP) and airflow (Q_f) available from the fan as follows:

$$\Delta P = 2 f_c \rho \left(\frac{Q_f}{nA}\right)^2 \times L_c \times D_h^{-1} + \frac{1}{2}\rho \left(\frac{Q_f}{nA}\right)^2 \quad (6)$$

$$f_c = (1.58 \ln R_e - 3.28)^2 \quad (7)$$

where ρ is the density of the air, R_e is the Reynolds number of the system and A is the area of the wedge-shaped regions between the fins (cooling passages) which can be defined as

$$A = \frac{\pi(r_{tube}^2 - r_{fo}^2)}{n} - tL_{fin} \quad (8)$$

where r_{tube} is the inner radius of the motor cooling system and can be written as

$$r_{tube} = L_{fin} + r_{fo} \quad (9)$$

D_h is the hydraulic diameter of the cooling passages, which is written as:

$$D_h = \frac{4\left[\frac{\pi(r_{tube}^2 - r_{fo}^2)}{n} - tL_{fin}\right]}{\frac{2\pi}{n}(r_{tube} + r_{fo}) + 2(L_{fin} - t)} \quad (10)$$

Since the Reynolds number of the system is around 8000 and the flow is transitional, the recent revisions [18] to the classic Gneilinski correlations for turbulent tube flow for the annular tube with a hydraulic diameter of D_h were used to estimate the heat transfer coefficient h_{fin}.

Heating the magnet causes reversible demagnetisation and weakens its magnetic field. Furthermore, heating the coil increases its electrical resistivity. Therefore, to compensate for these effects the motor has to produce a compensating power (P_A), which can be written as

$$P_A = P\frac{1 + P_A R_{th,tot}\alpha_c}{(1 + P_A R_{th,tot}\alpha_m)^2} \quad (11)$$

where α_c is the temperature coefficient of the coil resistance and α_m is the temperature coefficient of the remanence.

Using the thermal model of the motor (5), the temperature rise in the motor and the maximum temperature of the motor can be written as

$$\Delta T = R_{th,tot} P \quad (12)$$

$$T_{max} = \Delta T + T_{outlet} \quad (13)$$

where T_{outlet} is the temperature of the air exiting the motor and can be written as

$$T_{out} = T_{in} + \frac{P}{Q_f \rho C_{air}} \quad (14)$$

where T_{in} is the temperature of the inlet air and C_{air} is the specific heat capacity of the air.

B. Motor optimization

The design specification of our assistive robot dictates that the motor is required to have a minimum contracted length of 248.8 mm and stroke of 131 mm while safely providing 100 N of force [13]. The objective of the motor design is to find the motor parameters including the repeat unit length of the motor, number of coil and magnet periods, diameter and thickness of the coil, magnet and back-iron, number and length of the cooling system fins, that satisfy these requirements. The overall optimisation consists of a strategic repetition of the inner optimization loop to minimise the mass of the motor (M).

In the optimisation process, an outer loop performs a grid search for a pair of N_C and N_M. These values are passed to the inner loop where a constrained nonlinear multi-variable optimization based on the interior point algorithm (MATLAB Optimization Toolbox) is used to minimise the mass of the motor subject to constraints on force and temperature.

Using the thermal model of the motor and allowing for a $40\,\%$ safety factor on the power to account for any model inaccuracies, a thermal constraint was defined to keep the maximum temperature of the motor below 80 °C and avoid demagnetisation of the magnet for ambient temperatures of up to 30 °C. An air flow rate of 12.5 L/s air flow at a pressure drop of 367 Pa was selected for the fan based on the datasheets of typical high-static-pressure fans which weigh less than 60 g.

In practice, creating a cylindrical Halbach array requires assembling small magnets, which repel one another. To allow the magnet array to serve as a motor bearing, a thin stainless-steel tube encloses the magnets while its outside slides against the bearing. Therefore, the magnet diameter was constrained to correspond to standard tubing sizes. The coil fill factor was assumed to be $62\,\%$, and a 1.1 mm radial gap between the coil and magnet and a 0.2 mm radial gap between the coil and back-iron tube was allowed for motor assembly. The motor was designed with N45SH magnets (1.34 T remanence), and the back-iron tube thickness was chosen to maintain the field within it below 2 T, avoiding saturation effects.

Following an initial optimisation, the number of coil periods was reduced to 4.5 to simplify the construction of the motor and another optimization was run. Comparing the results of both optimisations reveals that reducing the number of coil periods increased the motor mass by $1.8\,\%$ and decreased the power by $3.3\,\%$. The final optimised motor parameters are summarised in table I.

TABLE I
SUMMARY OF MOTOR MOTOR PARAMETERS

Parameters	Optimised Values
Nominal mass (g)	608.4
Nominal power (W)	99.5
Repeat length L_k (mm)	26.2
Radial magnet length (mm)	4.1
Magnet inner radius r_{mi} (mm)	2.0
Magnet outer radius r_{mo} (mm)	8.9
Coil inner radius r_{ci} (mm)	10
Coil outer radius r_{co} (mm)	11.8
Iron inner radius r_{fi} (mm)	12
Iron outer radius r_{fo} (mm)	13.1
Number of coil periods	4.5
Number of magnet periods	9.5
Back iron length (mm)	124.5

Following the design optimisation, a finite-element-analysis-based procedure was performed using ANSYS Mechanical APDL to adjust the length of the back-iron to minimise cogging force [8]. The cogging force was minimised by the addition of approximately 1/4 of a repeat unit length to the back-iron, resulting in a length of 124.5 mm. A similar finite element procedure was used to validate the semi-analytical model's performance estimates. This analysis supported the analytical model, predicting a motor constant between 9.54 N/W$^{-0.5}$ and 9.83 N/W$^{-0.5}$ (at the end and the middle of stroke, respectively) as compared to the analytically modelled value of 10.05 N/W$^{-0.5}$.

The performance of the motor at 80 °C was also evaluated. The coercivity, intrinsic coercivity and relative permeability of the N45SH magnets at 20 °C are 13 kOe, 21 kOe and 1.037 respectively. Using ANSYS Mechanical APDL, the ideal force that the motor can produce with 170 W of input power was found to be 124.4 N. In a separate analysis, the coercivity, intrinsic coercivity and relative permeability of the magnets were changed to 11.85 kOe, 13.25 kOe and 1.059 respectively, which correspond to N45SH magnet properties at 80 °C. Additionally, to account for permanent demagnetization, any elements in the finite element model exposed to an opposite magnetic field higher than the intrinsic coercivity were eliminated (coercivity set to zero). It was found that the motor operating at 170 W and 80 °C produces 115.26 N and thus the magnets are weakened by 7.3 %. The result also shows that only a small number of elements located at the corners of the magnets were permanently demagnetised as shown in Fig. 3. Therefore, the operating point of 80 °C is safe for the magnets and self-demagnetisation is not a significant issue for the actuator at this operating temperature.

III. Mechanical Design and Fabrication

The motor and its cooling system were incorporated into an actuator (Fig. 1). To fabricate the shaft of the motor, the array of magnets was located in a 0.3 mm thick stainless-steel tube and supported by a 3 mm stainless-steel rod and two plastic bushes at each end. The back-iron tube was machined from

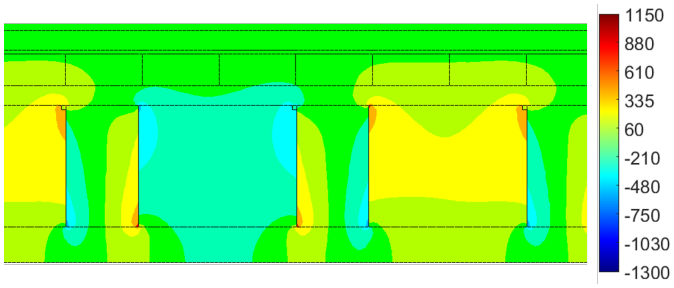

Fig. 3. The radial magnetic field intensity (kA/m) at the center of the motor is shown at 80 °C.

1080 carbon steel rod and was provided with a 3 mm slit to facilitate electrical connection of the coil. Two plastic linear bearings were machined from Rulon rod and connected to each end of the back-iron tube (Fig. 4).

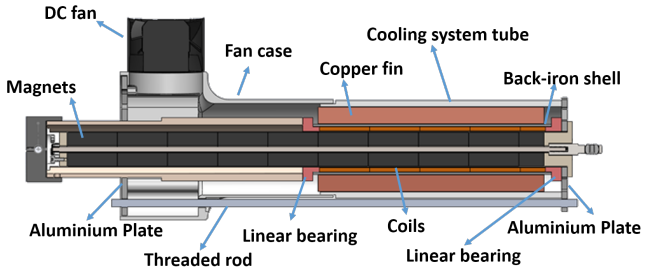

Fig. 4. Longitudinal cross-section of the actuator, showing the coil (light orange), magnet array (black), and structural elements.

To simplify the fabrication process and avoid using a thin bobbin for winding the coils, the air gap between the magnet and coil was reduced to 0.7 mm which allowed an increased mass of the copper coil by using a thicker bobbinless coil (visible in Fig. 5). Therefore, the nominal mass, and power of the motor changed to be 624 g and 80 W (30 VDC and 2.7 A), respectively, which subsequently increased the motor constant (predicted by semi-analytical model) to 11.18 N/W$^{-0.5}$. The final fabricated motor uses 27 bobbinless coils (5 layers and 9 turns each, 2.2 mm thickness), which were wound using single build 26 AWG copper magnet wire. Nine coils were connected through a circuit board (Fig. 5) in series to form each phase, resulting in a phase resistance of 3.6 Ω.

The motor uses a 40 mm high-static-pressure fan (Delta-FFB0412EN-00Y2E) connected to a 3D printed fan case to extract air from the motor. An array of 36 copper fins with an outer radius of 20 mm were fused to the back-iron tube and were enclosed in a tubular polycarbonate casing, as shown in Fig. 6.

To hold the structure of the motor stator, the back-iron tube was connected to a plastic tube and sandwiched between two aluminium plates by a set of three aluminium threaded rods, as shown in Fig. 4.

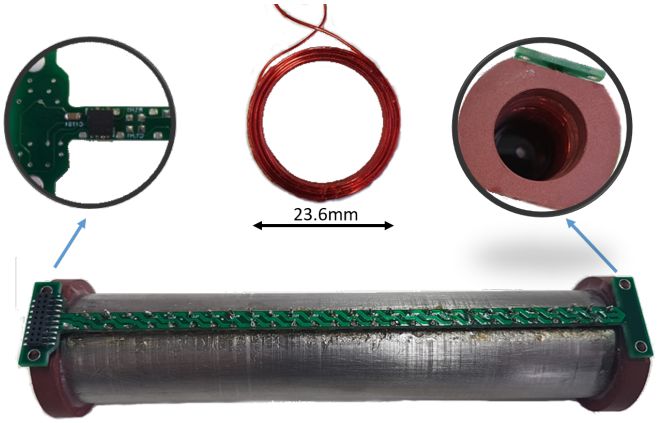

Fig. 5. Coil assembly, showing the back-iron and the circuit board.

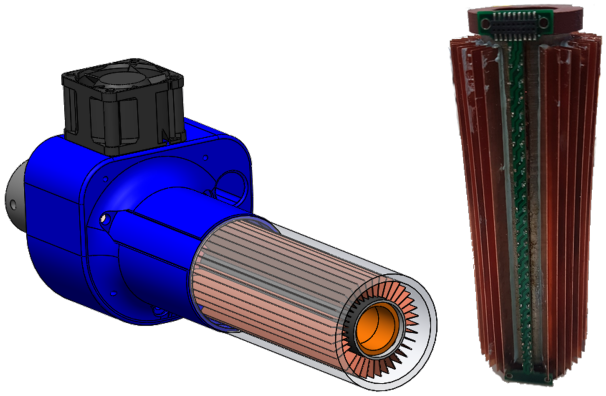

Fig. 6. The motor cooling system and fabricated fin array on the back-iron tube.

IV. Actuator Characterisation

The motor was driven with a manual six-step commutation switch from a DC power supply (KEITHLEY 22318A-30-3) with a maximum rated output current of 3 A. While this power supply cannot deliver the rated maximum power for the motor, it was sufficient for characterizing the thermal and electromagnetic performance. The switch was set to apply a positive DC current to one of the phases and negative DC current to the other two phases. A load cell (OMEGA LCM201-100N) was attached to the shaft of the motor and connected to a NI Compact RIO 9022 real-time system controlled with a LabVIEW interface. A digital temperature sensor (Microchip Technology TC72-3.3MMFTR) located on the motor circuit board (shown in Fig. 5) was connected to the outer surface of the first coil to monitor the temperature change of the coils during the experiment.

A. Static performance of the motor

The motor was manually moved over its travel in both directions: once without applying power to the motor to characterise the friction and cogging force, and once while applying 9.3 W to the coil to measure the force production of the motor. The measured cogging and friction force was 9.5 N in both directions. With 9.3 W of input power the motor produced 29.9 N of force, which corresponds to a motor constant of 9.82 N/W$^{-0.5}$.

However, this method potentially was susceptible to error as the applied manual force to the load cell was not perfectly axial and hence the sensor might show a higher value resulting in higher motor constant. Therefore, in a separate experiment, using the compact RIO, the phase voltage constants of the motor was also measured (Fig. 7) while externally-induced motion was applied to the the shaft of the motor. A digital linear incremental optical encoder (MicroE Optira PIA-5000-A0-02-A) with a resolution of 5 μm was used to record the position and the instantaneous velocity of the motor shaft while the induced back EMF (electromotive force) voltages in the motor phases were instantaneously measured.

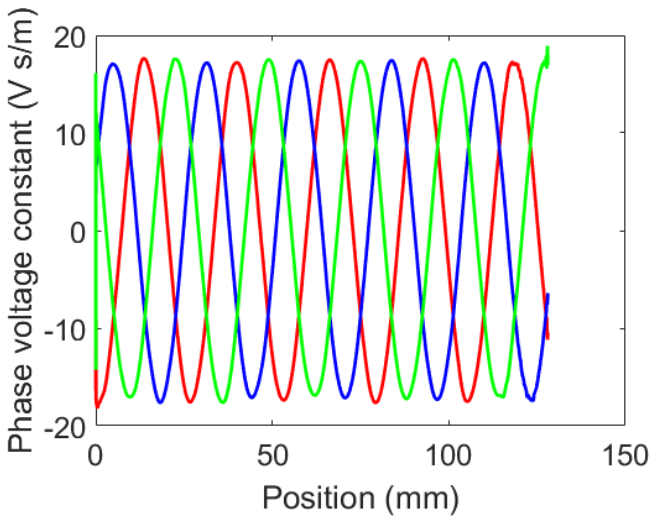

Fig. 7. Averaged measured phase voltage constants against motor position, determined over multiple passes at different velocities up to 280 mm/s.

Based on the peak measured voltage constant for the three phases and the phase resistance of the motor, the motor constant was evaluated to be 9.21 N/W$^{-0.5}$ which is about 6 % less than than the first method and 17 % below the analytical model prediction. The reduced performance seen in the motor compared to the analytical model is likely to be due to a reduced winding fill factor of coils during the fabrication process as compared to that expected.

B. Thermal performance of the motor

To test the thermal performance of the motor, the power dissipation was varied with the coil in a fixed position while the temperature changes in the coil were recorded (Fig. 8). The measured temperature was normalised to the initial value that sensor reported at 0 W of power. As shown in Fig. 8, the measured temperature rise is $\sim$ 50 % higher than the prediction of the analytical model. However, considering the safety factor used in designing the motor, the cooling system is still able to dissipate 80 W of power from the motor and keep the maximum temperature of the motor under 80 °C.

The difference between the measured temperature and the analytical model is likely due to the presence of an air gap between the coil and back-iron tube during manufacturing the device, which led to hot spots in the coil. Moreover, since the temperature sensor is located close to the circuit board connector, it may be influenced by local power dissipation in the connector and circuit board components.

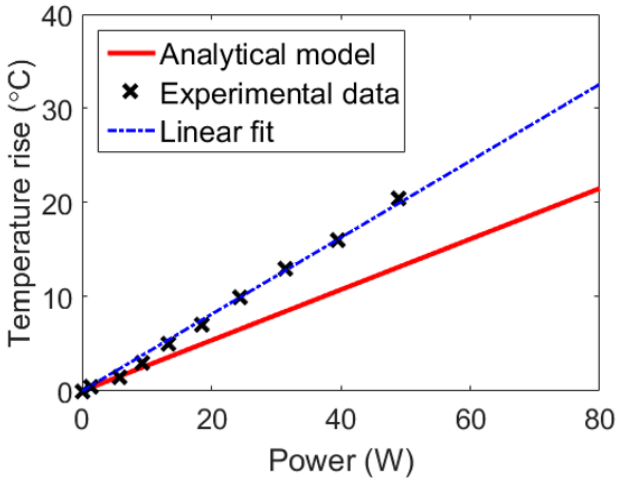

Fig. 8. Comparison of the measured temperature rise of the motor with the analytical model for the room temperature of 22.4 °C.

V. CONCLUSIONS

We have presented the design and fabrication of an actively air cooled direct-drive linear actuator for a wearable assistive robot. We used a semi-analytical electromagnetic model and a thermal model of the linear actuator to minimise the mass of the motor. The final prototyped motor employs an aggressive active cooling scheme to remove the heat from the motor, allowing the motor to safely operate up to 80 W of power and to keep the maximum temperature of the motor under 80 °C. The static and thermal performances of the motor were tested and were found to agree well with the predicted models, suggesting the motor can achieve a high continuous force density of $\sim$ 132 N/kg. As such, this work opens an opportunity for the use of direct-drive linear motors in wearable robots where the mass and size of the motor are the main constraints. Work is underway to fabricate an assistive robot using this linear actuator so that it can be tested with human participants.

ACKNOWLEDGMENT

The authors wish to thank Dr Paul Roberts for his help with assembling the actuator.

REFERENCES

[1] J. Mehrholz, M. Pohl, T. Platz, J. Kugler, and B. Elsner, "Electromechanical and robot-assisted arm training for improving activities of daily living, arm function, and arm muscle strength after stroke," *The Cochrane Library*, no. 9, 2018, Art. no.: CD006876.

[2] R. E. Cowan, B. J. Fregly, M. L. Boninger, L. Chan, M. M. Rodgers, and D. J. Reinkensmeyer, "Recent trends in assistive technology for mobility," *Journal of neuroengineering and rehabilitation*, vol. 9, no. 1, p. 1, 2012.

[3] J. McBean and C. Breazeal, "Voice Coil Actuators for Human-Robot Interaction," in *2004 IEEE/RSJ International Conference on Intelligent Robots and Systems (IROS)*, Sendai, Japan, 2004.

[4] A. Schiele, "Fundamentals of ergonomic exoskeleton robots," Ph.D. dissertation, TU Delft, 2008.

[5] B. P. Ruddy and I. W. Hunter, "Design and optimization strategies for muscle-like direct-drive linear permanent-magnet motors," *The International Journal of Robotics Research*, vol. 30, no. 7, pp. 834–845, 2011.

[6] I. A. Smadi, H. Omori, and Y. Fujimoto, "Development, analysis, and experimental realization of a direct-drive helical motor," *IEEE Transactions on Industrial Electronics*, vol. 59, no. 5, pp. 2208–2216, 2012.

[7] N. C. Hogan, A. J. Taberner, L. A. Jones, and I. W. Hunter, "Needle-free delivery of macromolecules through the skin using controllable jet injectors," *Expert opinion on drug delivery*, vol. 12, no. 10, pp. 1637–1648, 2015.

[8] N. N. L. Do, A. J. Taberner, and B. P. Ruddy, "Design of a linear permanent magnet synchronous motor for needle-free jet injection," in *2017 IEEE Energy Conversion Congress and Exposition (ECCE)*, Cincinnati, Ohio, 2017, pp. 4734–4740.

[9] M. Galea, C. Gerada, T. Raminosoa, and P. Wheeler, "A thermal improvement technique for the phase windings of electrical machines," *IEEE Transactions on Industry Applications*, vol. 48, no. 1, pp. 79–87, 2011.

[10] Z. Xu, A. Al-Timimy, M. Degano, P. Giangrande, G. L. Calzo, H. Zhang, M. Galea, C. Gerada, S. Pickering, and L. Xia, "Thermal management of a permanent magnet motor for an directly coupled pump," in *2016 XXII International Conference on Electrical Machines (ICEM)*, Lausanne, Switzerland, 2016, pp. 2738–2744.

[11] B. P. Ruddy and I. W. Hunter, "A compact direct-drive linear synchronous motor with muscle-like performance," in *2013 IEEE International Conference on Robotics and Automation (ICRA)*. Karlsruhe, Germany: IEEE, 2013, pp. 1498–1503.

[12] G. M. Gilson, T. Raminosoa, S. J. Pickering, C. Gerada, and D. B. Hann, "A combined electromagnetic and thermal optimisation of an aerospace electric motor," in *2010 XIX International Conference on Electrical Machines (ICEM)*, Rome, Italy, 2010, pp. 1–7.

[13] S. Haji Hosseinnejad, T. F. Besier, A. J. Taberner, and B. P. Ruddy, "Design optimization of a direct-drive linear actuator assistive device for stroke," in *2017 IEEE/RSJ International Conference on Intelligent Robots and Systems (IROS)*, Vancouver, Canada, 2017, pp. 6349–6354.

[14] B. P. Ruddy, A. J. Taberner, and J. Boyce-Bacon, "Optimization of linear permanent magnet synchronous motors for needle-free jet injection," in *2015 Intl Aegean Conference on Electrical Machines & Power Electronics (ACEMP), 2015 Intl Conference on Optimization of Electrical & Electronic Equipment (OPTIM) & 2015 Intl Symposium on Advanced Electromechanical Motion Systems (ELECTROMOTION)*, Side, Turkey, 2015, pp. 375–381.

[15] J.-M. Jin, *The finite element method in electromagnetics*. John Wiley & Sons, 2015.

[16] N. Bianchi, "Analytical field computation of a tubular permanent-magnet linear motor," *IEEE Transactions on Magnetics*, vol. 36, no. 5, pp. 3798–3801, 2000.

[17] Wijono, H. Arof, and H. W. Ping, "Analysis of magnetic field distribution of a cylindrical discrete Halbach permanent magnet linear generator," *IET Electric Power Applications*, vol. 4, no. 8, pp. 629–636, 2010.

[18] V. Gnielinski, "On heat transfer in tubes," *International Journal of Heat and Mass Transfer*, vol. 63, pp. 134–140, 2013.